TOPICAL REVIEW

Recent advances in Rydberg physics using alkaline-earth atoms

IOP Publishing Journal of Physics B: Atomic, Molecular and Optical Physics
J. Phys. B: At. Mol. Opt. Phys. **49** (2016) 112003 (11pp) doi:10.1088/0953-4075/49/11/112003

Topical Review

Recent advances in Rydberg physics using alkaline-earth atoms

F B Dunning[1], T C Killian[1], S Yoshida[2] and J Burgdörfer[2]

[1] Department of Physics and Astronomy, Rice University, Houston, TX 77005-1892, USA
[2] Institute for Theoretical Physics, Vienna University of Technology, Vienna, Austria

E-mail: fbd@rice.edu

Received 25 January 2016, revised 16 March 2016
Accepted for publication 8 April 2016
Published 9 May 2016

Abstract

In this brief review, the opportunities that the alkaline-earth elements offer for studying new aspects of Rydberg physics are discussed. For example, the bosonic alkaline-earth isotopes have zero nuclear spin which eliminates many of the complexities present in alkali Rydberg atoms, permitting simpler and more direct comparison between theory and experiment. The presence of two valence electrons allows the production of singlet and triplet Rydberg states that can exhibit a variety of attractive or repulsive interactions. The availability of weak intercombination lines is advantageous for laser cooling and for applications such as Rydberg dressing. Excitation of one electron to a Rydberg state leaves behind an optically active core ion allowing, for high-L states, the optical imaging of Rydberg atoms and their (spatial) manipulation using light scattering. The second valence electron offers the possibility of engineering long-lived doubly excited states such as planetary atoms. Recent advances in both theory and experiment are highlighted together with a number of possible directions for the future.

Keywords: Rydberg atoms, atomic physics, ultracold atoms

(Some figures may appear in colour only in the online journal)

Rydberg atoms provide an excellent vehicle with which to study strongly interacting quantum systems due to their long-range interactions. Such interactions can give rise to a number of interesting effects including dipole blockade in which multiple Rydberg excitations within some blockade sphere are inhibited due to the level shifts induced by the first Rydberg atom created. Dipole blockade can be exploited to entangle particles leading to creation of 'superatoms' and for quantum gate operations and quantum state engineering [1–5]. Blockade also allows formation of highly correlated many-body states [6] that can exhibit long-range crystalline order [7, 8] and can modify atom–light interactions giving rise to cooperative optical effects [8, 9]. In optical dressing, radiation tuned near resonance with the transition to a Rydberg state mixes a controllable amount of Rydberg character into the ground-state wave function. This allows control of atom–atom interactions by varying the strength of the optical dressing [10–14].

Many advances in Rydberg physics have been achieved using alkali atoms. However, recently there has been increasing interest in alkaline-earth Rydberg atoms which provide an opportunity to study new aspects of Rydberg physics. In particular, the presence of two valence electrons admits, within a single element, the production of both singlet and triplet states and of Rydberg states that can exhibit a variety of attractive or repulsive interactions. The availability of weak intercombination lines is advantageous for laser cooling and for applications such as Rydberg dressing [12, 13], generating spin-squeezed states [15], and atomic clocks [16, 17]. Furthermore, the presence of a pair of valence electrons leaves an optically active core ion after excitation of one of the electrons to a Rydberg state. For low-L states, excitation of the inner valence electron leads to autoionization which can be used to detect such states and to study time-resolved electron–electron collisions [18]. For high-L states, the inner valence electron can be excited without inducing

autoionization allowing the evolution of low-L states toward high-L states to be monitored as well as the optical imaging of Rydberg atoms and their (spatial) manipulation using light scattering. Optical transitions in the core ion can be used for magic wavelength optical trapping of Rydberg atoms [19]. The second valence electron also admits the possibility of engineering long-lived doubly excited states in the planetary atom or frozen planet configurations [20–23].

Initial studies of alkaline-earth Rydberg atoms used a variety of elements including barium, calcium, and strontium, and focused on the perturbation of a Rydberg series introduced by interactions with neighboring doubly excited states or an underlying continuum and, motivated by fundamental interest in the three-body Coulomb problem, on autoionization [24]. More recently, interest in alkaline-earth Rydberg atoms has expanded to include time-dependent studies of the dynamics of autoionization, high-resolution spectroscopy, measurements of quantum optical phenomena such as Autler–Townes splitting and electromagnetically induced transparency (EIT), production of ultra-long-range Rydberg molecules, exploration of Rydberg dressing, and the creation of ultracold plasmas. Recognizing that it is impossible to review all the earlier work with alkaline-earth Rydberg atoms in a short article, we restrict discussion here to recent results obtained using (principally) strontium Rydberg atoms that illuminate opportunities for the future. However, other alkaline-earth and alkaline-earth-like species such as ytterbium can be used to explore much of the same physics.

1. Experimental considerations

Strontium possesses four stable isotopes, three of which, ^{84}Sr, ^{86}Sr, and ^{88}Sr, are bosonic and one, ^{87}Sr, fermionic. The most abundant isotope is ^{88}Sr (82.88%) followed by ^{86}Sr (9.86%), ^{87}Sr (7.00%), and ^{84}Sr (0.56%). We focus on the bosonic isotopes which have zero nuclear spin and hence no ground-state hyperfine structure, thereby greatly simplifying their excitation spectra. Beams of strontium atoms can be produced using an oven. However, the vapor pressure of strontium is significantly lower than that of the heavier alkali metals requiring the use of higher oven temperatures, ~400 °C–600 °C, to achieve beam densities $\sim 10^9$ cm^{-3}. Strontium Rydberg atoms can be detected using conventional techniques such as field ionization or ionization induced by collisions (Penning ionization) or blackbody-radiation-induced photoionization as well as by autoionization resulting from excitation of the core ion.

Figure 1 shows a partial term diagram for strontium that includes the atomic levels and transition wavelengths pertinent to the present discussion. Singlet n^1S_0 and n^1D_2 Rydberg atoms can be conveniently created by two-photon excitation via the intermediate 5s5p $^1P_1$ state, radiation at the required wavelengths being readily generated using diode laser systems. Higher Rydberg production rates can be achieved by three-photon excitation to n^1F_3 and n^1P_1 levels using the 5s5p ^{1}P$_1$ and 5s5d $^1D_2$ intermediate states because diode laser systems can provide high output powers (>1W) at 893 nm for

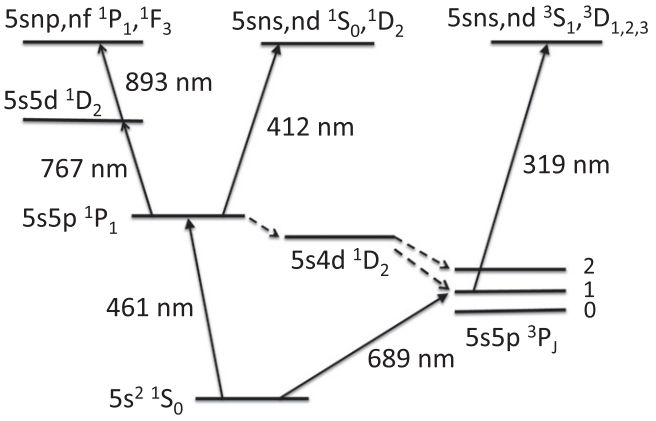

Figure 1. Partial strontium term diagram showing the transitions of interest in production of singlet and triplet Rydberg states.

the final excitation step. Two-photon excitation via the intermediate 5s5p $^3P_1$ state is used to generate n^3S_1 and $n^3D_{1,2}$ Rydberg states although the required radiation at 319 nm must be generated by second harmonic conversion.

Strontium is particularly amenable to laser cooling and trapping and all its isotopes have been cooled to quantum degeneracy [25]. Cooling generally proceeds in three steps. In the first step, atoms from a Zeeman slower are captured and cooled to milliKelvin temperatures using a magneto-optical trap (MOT) operating on the broad 'blue' 5s^2 $^1S_0$ -5s5p $^1P_1$ transition at 461 nm. Atoms in the upper $^1P_1$ level, however, can decay via the $^1D_2$ level into the metastable 5s5p $^3P_2$ state. Those $^3P_2$ atoms in weak-field-seeking M_J states become trapped in the MOT magnetic field leading to the build up of a sizable population in this 'reservoir' state. This population can be rapidly returned to the ground state by optical pumping into the shorter-lived ($\tau \sim 21$ μs) $^3P_1$ state via one of a number of intermediate states [25]. The atoms can be recaptured and further cooled into the microKelvin regime using a 'red' MOT operating on the 5s^2 $^1S_0$-5s5p $^3P_1$ transition at 689 nm, its narrow linewidth resulting in a much lower recoil-limited temperature than can be achieved in a 'blue' MOT. These atoms can then be loaded into an optical dipole trap (ODT) and, once trapped therein, the 'red' MOT can be turned off and evaporative cooling used to increase the phase space density and achieve temperatures of ~100 nK and, ultimately, generate a Bose–Einstein condensate (BEC). ^{84}Sr is especially well suited to evaporative cooling due to its moderate scattering length $a \sim 123$ a$_0$, where a_0 is the Bohr radius. ^{86}Sr is also amenable to direct evaporative cooling although its larger scattering length, ~800a_0, requires use of large volume ODTs to obtain low atom densities and minimize three-body inelastic collision losses. ^{88}Sr is more challenging to cool due to its small negative scattering length $a \sim -2a_0$, which also results in collapse of the condensate above some critical atom number. Nonetheless, ^{88}Sr BECs have been produced by sympathetic cooling [26, 27]. ^{84}Sr atoms have been successfully loaded into optical lattices formed by three mutually orthogonal, retroreflected 532nm laser beams [25].

2. Theoretical considerations

The electronic structure of atoms is often discussed in terms of the interactions between the outermost 'active' electrons and a model potential that represents their interaction with the inner electrons. The alkalis can be well described by using a single-active-electron (SAE) model comprising a single electron moving in a model potential that incorporates the effect of core penetration by the valence electron. The situation for the alkaline earths is more complex as the excitation of one valence electron modifies the orbital of the second valence electron which leads to marked perturbations in the energy-level structure. For barium there is a complex interplay between a large number of perturber states in many different series, which provides a major challenge to theory [28]. However, there are only a few perturber states in strontium ($5p^2$, 4d5p, $4d^2$) that interact with low-n Rydberg levels. High-n singly excited 5snℓ states are therefore not affected by these perturbers and their wave functions near the core become independent of n due to the Coulomb potential $-Z/r$ becoming dominant over the binding energy $-1/(2n^2)$. (Unless otherwise noted atomic units are used throughout.) Quantum defect theory (QDT) builds on this and represents the core interaction as a nearly n-independent scattering phase shift (i.e., quantum defect) while the wave function outside the core region becomes a phase-shifted hydrogenic wave function (i.e., the superposition of regular and irregular Coulomb wave functions). Such core interactions can also be described using an SAE model that employs an n-independent (but ℓ-dependent) model potential that includes the influence of the second valence electron. Such SAE calculations can describe the wave functions outside the core region quite accurately allowing quantities such as transition matrix elements between high-n states to be readily calculated [29].

Simple QDT breaks down for low-lying n levels because electron–electron interactions become sufficiently strong to mix the orbitals of the second valence electron. For example, the strontium P and D states display relatively strong n dependences in their quantum defects. Such mixing can be taken into account by employing multichannel quantum defect theory (MQDT) [28, 30, 31] in which the eigenstates are a linear combination of several scattering channels. The admixture of regular and irregular wave functions in each channel, and the channels themselves, have to be chosen to satisfy the boundary conditions on the wave function. The parameters of the admixture are determined separately for each L-sector by fitting the results to measured data or, more rigorously, using R-matrix theory in which the wave functions inside the core region are calculated using a model potential to determine the fitting parameters.

Another approach to analyzing strontium electronic structure is a configuration interaction (CI) expansion of eigenstates using a two-active-electron (TAE) model [32] for which the Hamiltonian reads

$$H = \frac{p_1^2}{2} + \frac{p_2^2}{2} + V_{\ell_1}(r_1) + V_{\ell_2}(r_2) + \frac{1}{|\vec{r}_1 - \vec{r}_2|} \qquad (1)$$

where $V_{\ell_i}(r_i)$ is an angular-momentum-dependent semi-empirical potential representing the Sr^{2+} core ion. First, single particle orbitals $|\phi_{n_i}, \ell_i, m_i\rangle$ and orbital energies $E_{n_i\ell_i m_i}$ for the Sr^+ ion are generated with

$$H_{\rm ion} = \frac{p^2}{2} + V_\ell(r) \qquad (2)$$

These one-electron orbitals are used to construct basis states for the two-electron Hamiltonian that are symmetric (anti-symmetric) with respect to exchange to represent singlet (triplet) states and the eigenfunctions and eigenenergies calculated by numerical diagonalization. For an accurate calculation of the energy levels, spin–orbit coupling

$$\begin{aligned} V_{\rm LS}(r_1, r_2) \;=\; & \frac{1}{2}\alpha^2 \vec{s}_1 \vec{\ell}_1 \frac{1}{r_1}\frac{{\rm d}V_\ell(r_1)}{{\rm d}r} \\ & + \frac{1}{2}\alpha^2 \vec{s}_2 \vec{\ell}_2 \frac{1}{r_2}\frac{{\rm d}V_\ell(r_2)}{{\rm d}r}, \end{aligned} \qquad (3)$$

where $\vec{s}_1$ and $\vec{s}_2$ are the spin operators, is included to evaluate singlet-triplet mixing. For studies of single-electron excitation, a restricted set of orbitals for the inner valence electron can be used to reduce the size of the calculations. With such a limitation in the number of configurations the CI expansion becomes analogous to the MQDT/R-matrix approach. For TAE calculations, once the parameters of the model potentials are fit to the measured Sr^+ ion spectra, the eigenenergies of all L sectors can be calculated consistently. However, the available spectral data for the Sr^+ ion are limited resulting in some uncertainty in the model potential. Calculations show that excellent convergence in the spectra for singly excited states can be achieved using only six inner electron orbitals (5s, 4d, 5p, 6s, 5d, and 6p).

MQDT provides a versatile tool for analyzing energy levels of multi-electron systems when the parameters required to fit the measured data are known. The CI expansion requires larger computational effort but numerical diagonalization of the Hamiltonian yields directly the wave functions of the eigenstates. It is then straightforward to evaluate radial integrals and calculate quantities such as dipole matrix elements. This is advantageous for high-n states where the integration of regular and irregular Coulomb wave functions becomes challenging. With both low- and high-n wave functions at hand the oscillator strengths for excitation from the ground state (or other low-n states) to highly excited Rydberg states can be calculated allowing, for example, study of blockade effects in photoexcitation of Rydberg atoms and the lifetime of Rydberg states.

3. Spectroscopic studies

Initial spectroscopic studies of the alkaline-earths were designed to explore the perturbation of Rydberg series due to interactions with neighboring doubly excited states or an underlying continuum, as well as investigate autoionization [24]. These studies stimulated many of the advances seen in MQDT. More recently, spectroscopic measurements have been extended to cold ^{88}Sr gases allowing high-resolution

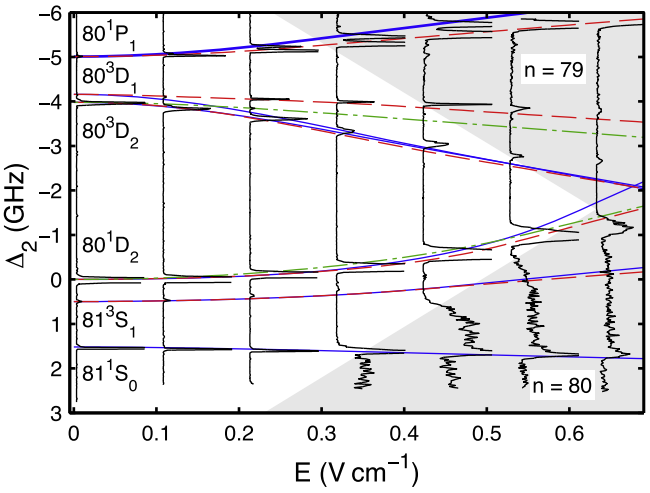

Figure 2. Stark spectrum for strontium in the vicinity of the 5s80d $^1D_2$ state. The solid black lines are experimental data recorded as a function of detuning Δ_2 from the zero-field 5s80d $^1D_2$ state. The blue (solid), red (dashed), and green (dot-dashed) lines show calculated $|M_J| = 0$, 1, and 2 levels, respectively. The shaded areas delineate the boundaries of the manifold of high-angular-momentum Stark states. Figure reproduced with permission from [33]. © 2011 IOP Publishing Ltd.

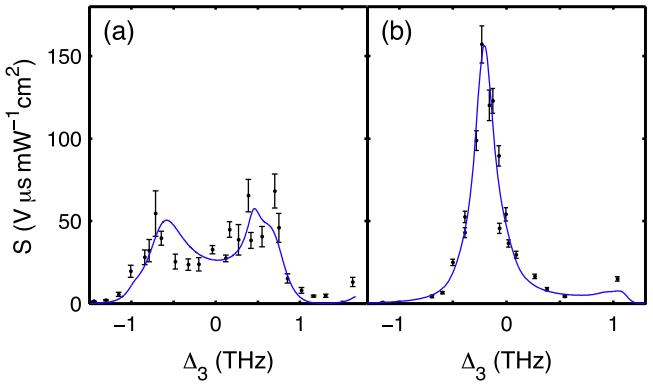

Figure 3. Autoionization spectra for (a) the 5s19d $^1D_2$ and (b) the 5s20s $^1S_0$ states of strontium. The lines show a fit using a six-channel MQDT model. Δ_3 is the detuning from the 5s $^2S_{1/2}$-5p $^2P_{3/2}$ core ion transition. Figure reproduced with permission from [33]. © 2011 IOP Publishing Ltd.

measurements [33]. The atoms were confined in a blue MOT equipped with electrodes to allow application of controlled electric fields and study of Stark spectra. The Rydberg atoms were created by two-photon excitation and were detected by measuring ions produced either through Rydberg collisions or through autoionization. The presence of the Stark field allowed observation of otherwise forbidden transitions to n^1P_1 states and the splitting of states into their component $|M_J|$ levels. Figure 2 shows a Stark map recorded in the vicinity of the 5s80d $^1D_2$ state. A number of singlet and triplet excited states are evident, each of which initially displays a quadratic Stark energy shift. Since the calculation of the Stark map requires the dipole matrix elements between Rydberg states, an SAE model is employed to calculate the energy shifts depicted in figure 2. The calculated energy levels are in excellent quantitative agreement with the experimental data, especially for the singlet states, and the interaction with the Stark manifold of higher-L states is well described.

Spectroscopic studies of autoionization induced by excitation of the 408 nm 5s $^2S_{1/2} \rightarrow$ 5p $^2P_{3/2}$ transition in the core ion were also undertaken, the autoionzation spectrum being measured by scanning the wavelength of the 408 nm laser [33, 34]. Representative autoionization spectra are shown in figure 3. The shapes and widths of the spectra depend strongly on the initial angular momentum ℓ of the Rydberg electron. The spectra were fitted using a six-channel MQDT model. Autoionization rates are governed by the oscillator strength for core excitation multiplied by the overlap between the initial bound and final autoionizing states associated with the outer electron. If the inner valence electron is essentially unperturbed by its interaction with the outer electron (isolated core excitation), the autoionization rate will simply depend on the difference $\epsilon = \delta_b$-δ_a between the quantum defect, δ_b, for the bound (Rydberg) state and that for the autoionizing state, δ_a. For $\epsilon \simeq 0$ (modulo-one) each Rydberg state only overlaps with a single autoionizing state resulting in a single peak in the autoionizing spectra, as seen for the 5s20s $^1S_0$ state for which $\epsilon = 0.15$. In contrast, for $\epsilon = 0.5$ (modulo-one) each Rydberg state overlaps with two autoionizing states and the autoionization spectrum becomes double-peaked as observed for the 5s19d $^1D_2$ state for which $\epsilon = 0.46$. The widths of these (low-n) autoionization features are large, $\sim$1 THz, and even for $n = 56$ remain $>$10 GHz indicating that autoionization is extremely rapid and can be used to probe the evolution of cold Rydberg gases with high temporal resolution.

The dynamics of autoionization have been explored using coherent short-pulse laser excitation [18]. Spectrally tailored picosecond laser pulses were employed to create radially localized Rydberg wave packets (in barium). Such radial wave packets 'breathe,' their radial coordinates expanding and contracting as time increases. Two radial wave packets were excited sequentially each of which left the vicinity of the nucleus at a well-defined time. These radial wave packets subsequently 'collided' as they passed through each other, the radius at which this collision occurred and thus the classical kinetic energy of the electrons at this time, being controlled by the time delay between their launches. Analysis of the data revealed that the energy transfer required to ionize the atom occurs in a single violent electron–electron collision rather than through a gradual exchange of energy between the electrons.

Spectroscopic measurements have been extended to very-high-n, $n \lesssim 500$, using a crossed laser–atom beam approach [32, 35, 36]. In initial experiments two-photon excitation via the 5s5p $^1P_1$ level was employed and the spectral resolution tested by measuring the isotope shifts in the high-n limit for the bosonic (strontium) isotopes. The spectra for each isotope were optimized by tuning the 461 nm laser to the specific wavelength required to excite $^1S_0$-$^1P_1$ transitions in that isotope. (Measurements with the ^{87}Sr isotope revealed strong hyperfine-induced singlet-triplet mixing and strong interactions between states of different n.) Of particular interest is the Stark spectrum and the excitation of extreme red-shifted

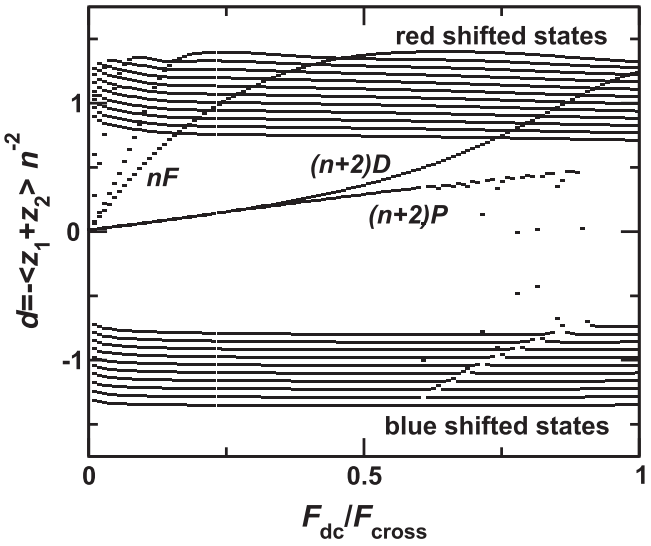

Figure 4. Calculated scaled dipole moments, $d = -\langle z_1 + z_2\rangle/n^2$ for selected $|M| = 1$ strontium Rydberg states with $n \sim 50$ expressed as a function of applied field normalized to the field, $F_{cross} = 1/3n^5$, at which states in neighboring manifolds first cross.

Stark states which is key to production of strongly polarized quasi-one-dimensional (quasi-1D) Rydberg atoms [36]. Such atoms have large electric dipole moments and form the starting point for many of the techniques developed to control and manipulate high-n states using one, or more, carefully tailored electric field pulses having characteristic times (duration, rise/fall times) $<T_n$, where T_n is the classical Kepler period (~4ns at $n \sim 300$) [37–39]. While initially developed using alkali Rydberg atoms, these techniques can be equally well applied to strontium for which the high-n states can be well described by an SAE model. Two independent methods for probing the polarization of the Stark states were evaluated. In each approach short probe pulses were used to ionize the atoms and the resulting ionization (or survival) probabilities mapped to the polarization, i.e., the electric dipole moment [35]. As seen in figure 2, the low-L non-degenerate Stark states initially display, to leading order, a quadratic Stark effect and are, at least in modest applied fields, only weakly polarized. However, because L-mixing is weak, the oscillator strengths for their creation remain large. As the field is increased, the isolated low-L states evolve onto quasi-hydrogenic states that display a near-linear Stark effect and can be strongly polarized. These states, still labeled by their low-field angular momentum designation 'nL' represent, in fact, a superposition of many L states and, in consequence, their photoexcitation rates become small. This evolution towards quasi-1D states can be explored using a TAE model. Figure 4 shows the calculated scaled dipole moments $d = -\langle z_1 + z_2\rangle/n^2$ for selected $|M| = 1$ states in the vicinity of $n = 50$ as a function of applied field, F_{dc}, scaled to the field, $F_{cross} = 1/3n^5$, at which states in neighboring manifolds first cross. The calculations indicate that in fields $F_{dc} \sim 0.8F_{cross}$ 'nD' states should possess dipole moments ~1.0 to 1.2 n^2 a.u., a prediction confirmed experimentally. Application of a dc field, however, results in a marked decrease in the

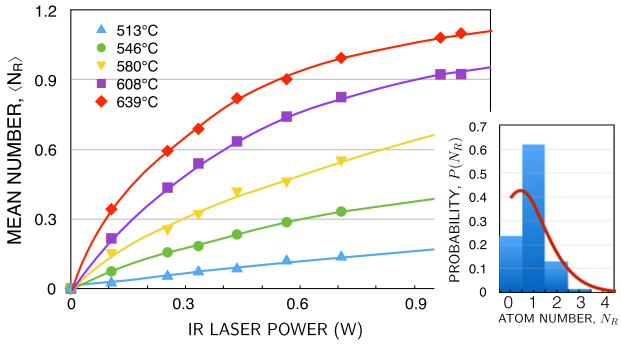

Figure 5. Mean number, $\langle N_R\rangle$, of $n = 310$ Rydberg atoms excited in a beam during a 130 ns long laser pulse as a function of 893 nm IR laser power for the oven operating temperatures indicated. The inset shows a typical measured Rydberg number distribution for $\langle N_R\rangle \sim 1$. The line indicates a Poissonian distribution for $\langle N_R\rangle = 1$.

Rydberg atom production rate and attention therefore shifted to three-photon excitation of 'nP' and 'nF' states [36]. Excitation in a field $F_{dc} \sim 0.3\ F_{cross}$ allowed production of ($n \sim 300$) 'nF' states with dipole moments of $\sim 1.2n^2$ and densities of $\sim 10^6$ cm^{-3}, even in a relatively low density ($\sim 10^9$ cm^{-3}) atomic beam.

In the absence of an electric field, n^1F_3 densities of $\sim 5 \times 10^6$ cm^{-3} were achieved corresponding to interatomic spacings of ~60 μm, below those required to study blockade effects in high-n atoms. Measurement of the number and number distribution of n^1F_3 atoms created in a small excitation volume defined using tightly focused crossed laser beams as a function of laser power and atom beam density revealed sizable blockade effects [40]. Figure 5 shows the mean number $\langle N_R\rangle$ of $n = 310$ Rydberg atoms created by a 130 ns-long laser pulse as a function of 893 nm laser power for several oven operating temperatures, i.e., beam densities. As $\langle N_R\rangle$ increases, the Rydberg production rate deviates from the linear dependence expected in the absence of blockade effects and the number distribution becomes increasingly sub-Poissonian with Mandel Q parameters, defined as

$$Q = \frac{\langle N_R^2\rangle - \langle N_R\rangle^2}{\langle N_R\rangle} - 1 \qquad (4)$$

as large as −0.55. As confirmed by theory, blockade, however, is not complete because van der Waals interactions between n^1F_3 Rydberg atoms are anisotropic, their strengths depending on the relative orientations of the atoms. Coupling of the target n^1F_3 pair with other (optically inaccessible) pairs, however, is sufficient to suppress excitation. Blockade promises creation of pairs of high-n Rydberg atoms with well-defined separations. Their mutual interactions might then be increased by using one, or more, electric field pulses to impulsively excite them to states of much higher n, the degree of coupling being tuned by varying the final target state (and interatomic spacing). Since the atoms are subject to the same pulse sequence, their initial electron motions are particularly well defined. The product two-electron wave packets provide an opportunity to explore energy interchange and ionization in the time domain and to search for long-lived configurations

where, due to their correlated motions, the electrons remain far apart.

The availability of high-resolution spectroscopic data stimulated development of new MQDT models for the S, P, D, and F singlet and triplet Rydberg series by fitting a reactance matrix [28]. These new models provided results in excellent agreement with experimental data and were employed to analyze the various Rydberg series in terms of channel fractions. Using these results, the Landé g_J factors for the $^1D_2$ and $^3D_2$ series were calculated demonstrating the effect of singlet-triplet mixing in the D_2 states, together with the lifetimes of the $^1S_0$ and $^1D_2$ states where perturbers were found to lower their lifetimes significantly.

4. Ultra-long-range Rydberg molecules

Scattering of the excited electron in a Rydberg atom from a neighboring ground-state atom can bind the two atoms together to form an ultra-long-range Rydberg molecule with internuclear separations on the order of the size of the Rydberg atom, i.e., $\sim n^2$. Such molecules represent a new type of chemical bond and can display surprising features like the presence of large permanent electric dipole moments, even in the case of a homonuclear molecule. Ultra-long-range Rydberg molecules, originally predicted theoretically [41], have now been observed in a variety of species. Initial experiments involved spherically symmetric Rb(nS) states [42, 43] and creation of molecules with small electric dipole moments but experiments have now been extended to include anisotropic nP and nD states [44–49] and, using Cs(nS) states, to creation of so-called 'trilobite' states that possess very large permanent electric dipole moments [50, 51]. In addition, molecules comprising one Rydberg atom and up to four ground-state atoms have been seen [52]. Detailed analysis of alkali data, however, is challenging due to the Rydberg electron spin–orbit and ground-state hyperfine interactions, which mix singlet and triplet electronic symmetries. For bosonic alkaline-earth atoms both these interactions are absent. Furthermore, electron scattering at ground-state rubidium and cesium atoms displays a strong p-wave shape resonance at low energies that further complicates the molecular structure and reduces the lifetime of Rydberg molecules (and Rydberg atoms) in a dense gas. Strontium, which does not possess a similar strong p-wave resonance, thus provides an attractive system for the study of Rydberg molecules as it allows straightforward, direct comparison between theory and experiment [53]. The long lifetimes in a dense gas make strontium attractive for the study of Rydberg atoms as impurities in quantum systems [54] which, given the interest in the physics of charged particles immersed in quantum-degenerate gases, promises to be an active area of future research [55].

Figure 6 shows an excitation spectrum recorded using a cold sample of ^{84}Sr atoms in the vicinity of the 5s38s $^3S_1$ Rydberg state, the excited atoms/molecules being detected by field ionization. The features evident to the red of the parent Rydberg peak result from the production of Rydberg

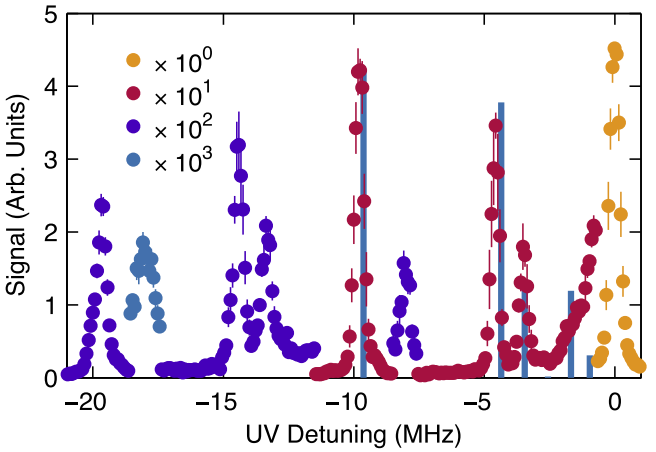

Figure 6. Rydberg excitation spectrum recorded using a dense cold-gas sample in the vicinity of the strontium 5s38s $^3S_1$ Rydberg state. The peak atom density is $\sim 5 \times 10^{13}$ cm^{-3}. Dimer peaks are indicated in red, trimer peaks in purple. The small remaining peak is attributed to tetramer formation. The calculated positions and relative excitation strengths for the dimer $v = 0$, 1, and 2 vibrational states are indicated by vertical bars.

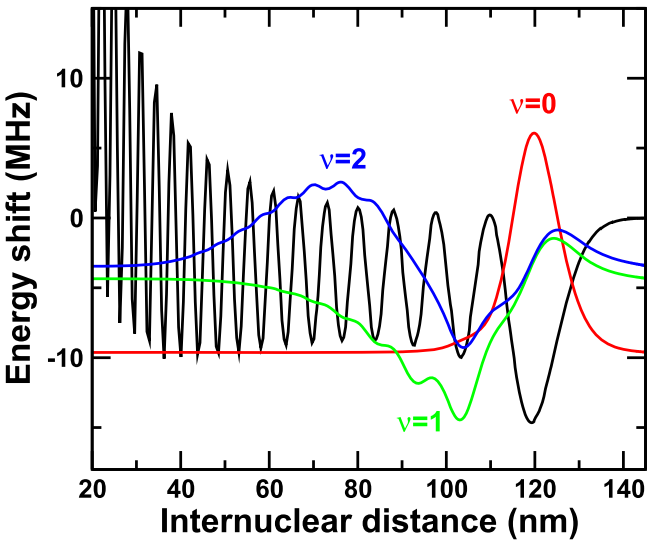

Figure 7. Calculated molecular potential for a 5s38s $^3S_1$-5s^2 $^1S_0$ strontium atom pair. The colored lines show the calculated wave functions $R\chi_v(R)$ for the $v = 0$ (red), 1 (green), and 2 (blue) molecular vibrational states.

molecules. The molecular potential calculated using a TAE model and first-order perturbation theory that utilizes a Fermi pseudopotential and effective s- and p-wave scattering lengths to describe the interaction between the excited electron and ground-state atom [53] is shown in figure 7 together with the calculated wave functions for the $v = 0$, 1, and 2 vibrational levels. The $v = 0$ wave function is strongly localized at large internuclear separations R in the outermost well of the molecular potential. The $v = 1$ wave function extends over several wells and penetrates to somewhat smaller values of R. The $v = 2$ wave function is even less well localized and extends to relatively small values of R. The calculated energy levels are included in figure 6 and are in good agreement with

the measured positions of the most prominent features as are the calculated relative excitation strengths. The experimental results also show the presence of a number of smaller features that result from the creation of trimer states comprising a parent Rydberg atom and two bound atoms. The binding energies of such states are given approximately by the sum of the separate binding energies of the two atoms, which depends on their vibrational states.

An interesting question concerning Rydberg molecules relates to their lifetimes and how these compare to the lifetime of the parent Rydberg atom. Studies using Rb(35s) parent atoms demonstrated that the lifetime of the parent atoms was significantly longer than that of the molecules, and that the lifetimes of the molecules themselves decreased with increasing vibrational excitation [56]. This behavior was attributed to the *p*-wave scattering resonance which results in a sharp decrease (step) in the molecular potential at relatively large internuclear separations. This allows the molecular constituents to move to small internuclear separations where interactions can lead to rapid destruction, although this is hindered by quantum reflection at the potential step resulting in reasonably long molecular lifetimes. As seen in figure 7, no such potential step is present at large internuclear separations for strontium, suggesting that, at least for the lower vibrational states, the lifetimes of the Rydberg molecules and parent atom should be equal which has now been confirmed experimentally [57]. This observation highlights the relative simplicity of the interactions involved in the formation of strontium Rydberg molecules and points to their future use to test theories of molecular formation free of the complexities associated with the alkali Rydberg molecules.

5. Rydberg dressing

Rydberg dressing can be used to control the interaction between 'ground-state' atoms [12–14, 58]. Theory predicts that such interactions can lead to a variety of interesting phenomena including creation of exotic spin and magnetic states [59, 60], three-dimensional solitons [61], and supersolids [10, 62, 63]. Studies of optical dressing of ^{84}Sr atoms contained in a cold gas or BEC have been undertaken using the dressing scheme shown in figure 8 which defines the relevant Rabi frequencies Ω_{01} and Ω_{12}, detunings δ_{01}, δ_{12}, and $\Delta = \delta_{01} + \delta_{12}$, and the decay rates γ_1 and γ_2. For weak dressing (i.e., $\delta_{01} \gg \Omega_{01}$ and $\Delta \gg \Omega_{\rm eff}$, where $\Omega_{\rm eff}$ is the effective two-photon Rabi frequency $\Omega_{01}\Omega_{12}/(2|\delta_{01}|)$), the dressed atomic ground state becomes

$$|g'\rangle = \left(1 - \frac{\Omega_{01}^2}{8\delta_{01}^2} - \frac{\Omega_{\rm eff}^2}{8\Delta^2}\right)|g\rangle + \frac{\Omega_{01}}{2\delta_{01}}|i\rangle + \frac{\Omega_{\rm eff}}{2\Delta}|r\rangle \qquad (5)$$

where $|g\rangle$, $|i\rangle$ and $|r\rangle$ denote the undressed ground, intermediate, and Rydberg states respectively. For large intermediate state detunings, $\delta_{01} \gg \Delta$, the intermediate state can be eliminated to reduce the system to a two-level atom [64]. For typical cold gas or BEC densities interactions between Rydberg atoms dominate, and are independent of the

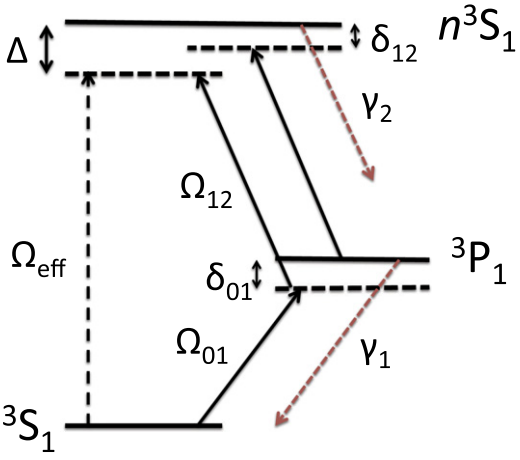

Figure 8. Schematic diagram of the dressing scheme employed in strontium showing the $^1S_0$ ground state, the intermediate $^3P_1$ state, and the n^3S_1 Rydberg state. The relevant Rabi frequencies Ω_{01} and Ω_{12}, $\Omega_{\rm eff}$ detunings δ_{01}, δ_{12} and Δ, and decay rates γ_1, γ_2 are as indicated.

population in the $|g\rangle$ or $|i\rangle$ state. Thus the interaction strength, which varies as $\Omega_{\rm eff}^2/4\Delta^2$, can be manipulated by varying $\Omega_{\rm eff}$ and Δ. Strontium atoms are attractive for studies involving Rydberg dressing because, when compared to alkali atoms, two-photon excitation to triplet Rydberg levels via the long-lived triplet intermediate state can reduce decoherence from light scattering for a given level of Rydberg coupling [10].

Measurements on ^{84}Sr cold-gas samples and BECs held in an ODT and dressed with the 5s30s $^3S_1$ state, however, demonstrate that dressing can lead to surprisingly large ground-state atom loss rates from the trap. This is illustrated in figure 9 which shows (for a BEC) the decrease in the number of ground-state atoms present in the trap as a function of overall detuning Δ following dressing by a series of N equally-spaced (by 100 μs) light pulses of duration $t_{\rm on}$, where the total dressing $N \times t_{\rm on}$ is kept constant to maintain similar peak trap losses. The widths of the trap loss features increase as $t_{\rm on}$ is increased (and N reduced). For a single pulse of 250 μs duration large trap losses are seen even when well detuned from resonance, i.e., even when the dressing is weak. Ground-state atom loss is attributed to the excitation of Rydberg atoms which can result in direct atom loss through recoil and in the population of the very-long-lived 5s5p $^3P_0$ and $^3P_2$ metastable states (which also constitutes a loss of ground-state atoms). As illustrated in the inset in figure 9, dressing with single pulses having durations $\lesssim$10 μs leads to only very small trap losses. Significant trap loss first becomes evident for pulse durations of ~25 μs and then increases rapidly with increasing pulse duration. This can be explained using a model in which the initial creation of a small number of 'seed' Rydberg atoms triggers 'avalanche-like' growth in the numbers of Rydberg atoms excited. At atom densities of ~10^{13}-10^{14} cm^{-3} the nearest-neighbor separations are much less than the blockade radius, a regime in which Rydberg–Rydberg interactions can lead to sizable energy shifts for subsequent excitations. In the case of n^3S_1 states which display isotropic, short-range repulsive interactions, excitation of a

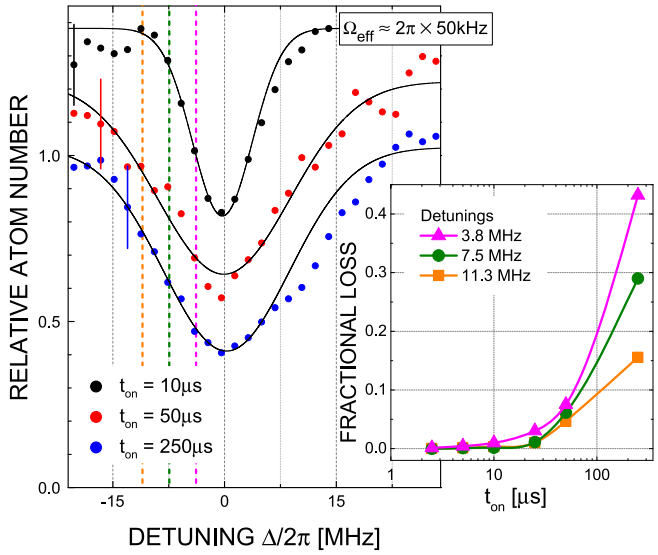

Figure 9. Measured relative decrease in the number of ground-state atoms present in an ^{84}Sr BEC containing ~5 × 10^5 atoms at a peak density of ~5 × 10^{13} cm^{-3} dressed with the 5s30s $^3S_1$ Rydberg state as a function of detuning for $\Omega_{eff} \sim 2\pi \times 50$ kHz. Dressing is provided in a series of N light pulses, each of equal duration t_{on} and separated by 100 μs, keeping the total dressing time N × t_{on} constant at 250 μs. The values of t_{on} employed are as indicated. The solid lines show Gaussian fits to the data at red detunings. The different profiles are offset by 0.2 on the vertical axis. The inset shows the trap loss per pulse for red detunings of ~3.8, 7.5, and 11.3 MHz as a function of pulse duration.

single Rydberg atom then allows, for blue laser detunings, resonant excitation of neighboring (ground-state) atoms to Rydberg states [65, 66]. Whereas such a process cannot account for the losses seen when red detuned, creation of 30^3S_1 atoms can also lead to population of neighboring high-n $n^3P_{0,1,2}$ states through blackbody-radiation-induced transitions or superradiance. High-n ^{3}P states interact strongly with 30^3S_1 Rydberg atoms resulting in the creation of both red- and blue-shifted pair states whose energy shifts are, for a given internuclear separation, much larger than for a pair of 30^3S_1 atoms. ^{3}P atom formation, therefore, enables the resonant excitation of even relatively distant ground-state atoms to the 30^3S_1 Rydberg level for both red and blue laser detuning. Enhanced Rydberg atom production, in turn, leads to creation of additional high-n ^{3}P atoms which further accelerates trap loss accounting for the large losses seen for the longer pulse durations, t_{on}. It should be noted that experiments with dressed alkali atoms have revealed unexpectedly large interaction-induced broadening [67–70] which was also explained in terms of dipole-dipole interactions with neighboring P states [69].

Trap losses severely limit both the strength and the duration of the dressing that can be applied. The effects of dressing, however, have been observed in systems with many fewer atoms [14, 71]. Nonetheless, if effects due to dressing are to be seen, small sample sizes and/or short time scales may be essential.

6. Rydberg–Rydberg interactions

As noted above, the generation of controlled unitary interactions in large ensembles through Rydberg dressing is challenging because of the large loss and dephasing rates seen experimentally. Rydberg blockade and Rydberg dressing in dense gases has been studied with two-photon excitation of alkali atoms in a three-level ladder configuration where, depending as to the relative excitation strengths of the two lasers employed, three different regimes can be accessed corresponding to coherent population trapping (CPT) [72, 73], electromagnetically-induced transparency (EIT) [9, 73], and Autler–Townes (AT) spectroscopy [74]. Alkaline earths, with their long-lived intermediate $^3P_1$ states, facilitate AT spectroscopy of strongly driven Rydberg transitions under conditions where the Rydberg state population is small, i.e., under conditions similar to those in EIT experiments performed using the alkalis.

Figure 10 shows the results of dressing a sample of ^{84}Sr atoms held in an ODT with the 5s24s $^3S_1$ Rydberg state via the intermediate 5s5p $^3P_1$ state [75]. (The lifetime of the 24^3S_1 state, ~4 μs, is significantly smaller than that of the $^3P_1$ state, ~21μs.) The 319 nm laser is tuned on resonance, $\delta_{12} = 0$ and provides a Rabi frequency $\Omega_{12}/2\pi = 2.4$ MHz. The 689 nm laser is scanned between detuning limits $\delta_{01}/2\pi$ of ±2 MHz and is chopped to provide optical pulses of 2 μs duration. The fraction of ground-state atoms remaining in the trap after one such pulse is shown in figure 10 as a function of the detuning of the 689 nm laser for the Rabi frequencies Ω_{01} indicated. For the smallest value of Ω_{01} an almost symmetrical AT spectrum is observed, typical of a non-interacting gas. As Ω_{01} is increased, shifts and asymmetries appear in the spectra pointing to increased interactions. To explain this behavior a density-matrix model was developed based on a one-body description. Many-body effects were averaged over and included as nonlinear energy shifts and dephasing rates that depend on the Rydberg density. A short-range cut-off in Rydberg–Rydberg separations set by the blockade radius for the van der Waals interaction is assumed to obtain finite values in the mean-field approximation of the shifts. The model results included in figure 10 assume that the nonlinear shift and dephasing rate are of equal magnitude. The reasonable agreement with the experimental data, especially for the lower values of Ω_{01}, highlights the important role played by blockade effects. As Ω_{01} is increased, clear signatures of increased dephasing appear through the broadening of the lines and increased atom loss on line center. To explore this, measurements were undertaken for longer excitation times, and data recorded for an exposure time of ~7 μs are included in figure 10. The atom loss spectrum is changed dramatically, collapsing to a single peak near the center of the line. This total loss of coherence of the dressed state implies dephasing on a time scale that is much shorter than the Rabi period and dephasing rates that are much larger than seen for short exposure times. However, related work suggests that under appropriate conditions the interplay between coherent light coupling, radiative decay, and strong Rydberg–Rydberg interactions can result in the emergence of sizable effective

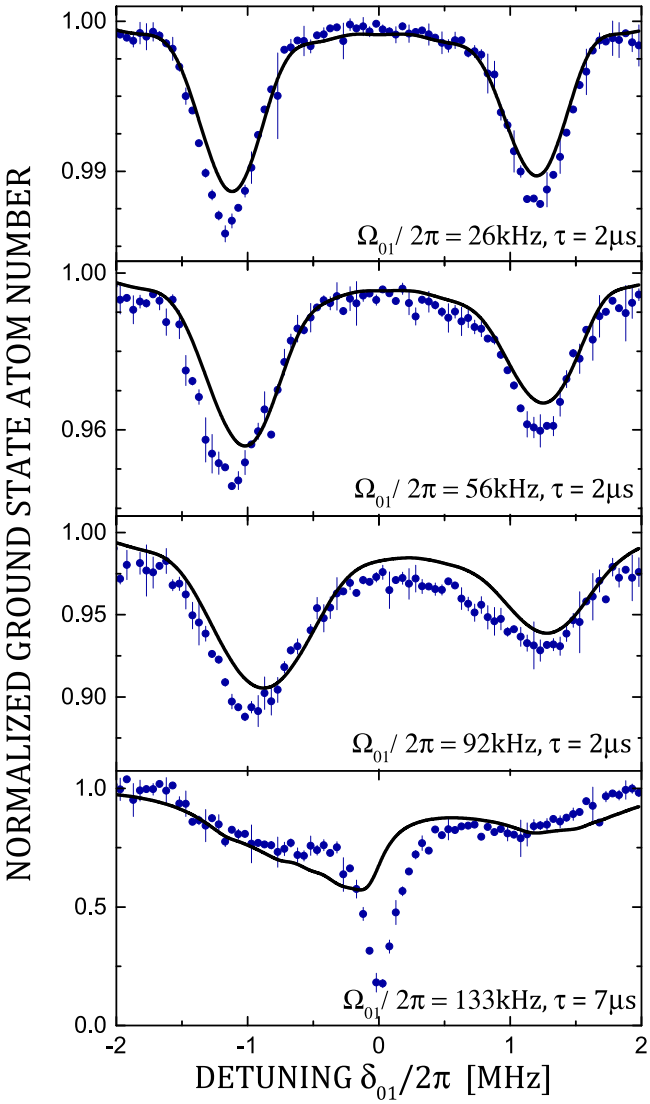

Figure 10. Normalized number of ground-state atoms remaining in the ODT after a single laser excitation pulse as a function of detuning δ_{01} for an initial peak density $\sim 1 \times 10^{13}$ cm^{-3} and the values of Ω_{01} and exposure times τ indicated (see text). The solid line shows the results of calculations using a density matrix approach accounting for interaction-induced level shifts and dephasing. Imaged reproduced with permission from [75]. © 2016 American Physical Society.

interactions while providing remarkably long coherence times [76]. The possibility of engineering atomic interactions under Rydberg EIT conditions offers new opportunities to probe the coupled nonlinear dynamics of light and matter wave fields.

7. Ultracold neutral plasmas

Excitation of a cold gas to Rydberg states can lead to collisions and Penning ionization, triggering a collisional cascade that can spontaneously transform a Rydberg gas into an ultracold neutral plasma [77–79]. Most earlier experimental studies of such evolution utilized laser cooled alkali or alkali-like atoms including rubidium, cesium, and metastable xenon. The principal diagnostic employed was the detection of charged particles that escaped the plasma or that were stripped from the atoms (or plasma) by an applied field. While selective field ionization (SFI) provides a measure of state selectivity, it provides no spatial resolution unless, for example, used with highly-magnifying charged particle optics [80]. For the alkaline-earths, however, the scattering of resonant light off the core ions can provide spatially and temporally resolved *in situ* imaging. Such laser-induced fluorescence (LIF) provides a valuable tool with which to follow the evolution and collisional dynamics of Rydberg populations.

The power of this technique has been demonstrated using ^{88}Sr atoms initially held in a 'blue' MOT and excited to either the 5s48s $^1S_0$ or 5s47d $^1D_2$ state [81]. The core ions were imaged using the 5s $^2S_{1/2}$-5p $^2P_{1/2}$ transition at 422 nm. Figure 11 shows the spontaneous evolution of the number of visible core ions as a function of time following excitation of $\sim 10^6$ $^1S_0$ or $^1D_2$ Rydberg atoms in a 'cigar-shaped' cloud with dimensions of $\sim 1 \times 3$ mm. These images provide a sensitive spatially resolved probe of the collision dynamics, i.e., whether or not the parent Rydberg atoms remain in their initial low-L states for which core ion excitation would lead to autoionzation rather than to fluorescence. Transitions to high-L states induced by 'ℓ-changing' Rydberg–Rydberg collisions, or in collisions with low-energy electrons liberated through Penning ionization, renders the core ions visible, as does Penning ionization or electron impact ionization. As seen in figure 11, while the general characteristics of the evolution of the $^1S_0$ and $^1D_2$ clouds are similar, i.e., visibility starts in the densest regions and propagates in space and time to encompass the entire cloud, the timescale for this evolution is noticeably slower for the $^1D_2$ cloud. This is explained by noting that interactions between the $^1S_0$ states are attractive whereas those between $^1D_2$ states are largely repulsive.

Core ion imaging allows detailed study of the dynamics governing the evolution of an ultracold gas of Rydberg atoms, in particular of the L-changing collisions that occur during the early stages of the evolution. Furthermore, it was shown that the introduction of low-energy 'seed' photoelectrons leads to rapid ionization providing a means to determine the total number and density of Rydberg atoms present at the time of their introduction. LIF can provide high time resolution, $\sim$10 ns, and, as seen in figure 11, spatial resolutions of $\sim$200 μm are readily achievable, although these could be substantially improved by use of better optics. LIF should be particularly valuable for imaging spatial correlations such as might arise from dipole blockade in a one- or two-dimensional ODT. Dipole blockade has been proposed as a way to create even colder ultracold neutral plasmas as it allows excitation of an ordered array of Rydberg atoms which can then be ionized using 'seed' electrons resulting in the production of an ordered array of core ions which would greatly reduce subsequent disorder-induced heating [82]. The plasma temperature might also be reduced by laser cooling the core ions using the 5s $^2S_{1/2} \rightarrow$ 5p $^2P_{1/2,3/2}$ transitions [83]. Furthermore, divalent atoms allow for relatively straightforward ionization of their singly charged ions. This has been studied

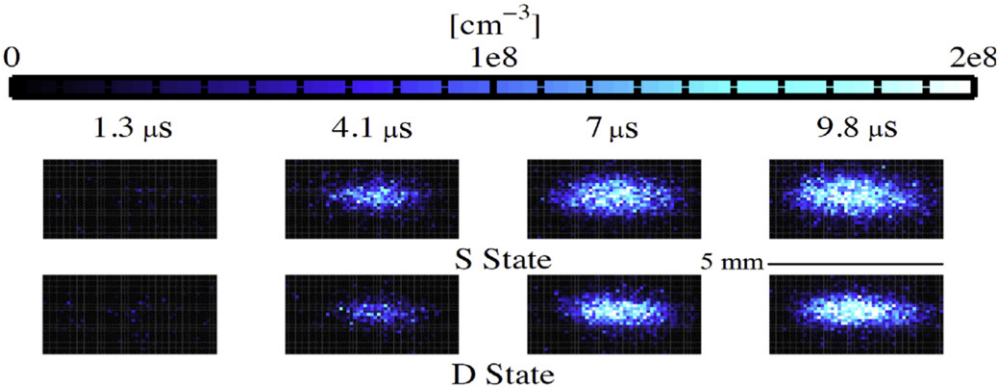

Figure 11. LIF images showing the spontaneous evolution of the density of visible core ions in an ultracold gas of 5s48s $^1S_0$ (top) and 5s47d $^1D_2$ (bottom) Rydberg atoms. The density color scale and the evolution times are indicated at the top. The initial Rydberg numbers and density distributions for both Rydberg species are identical (see text).

with calcium as a possible way to form more strongly interacting ultracold plasmas [84].

8. Summary

Interest in the alkaline-earth atoms has increased rapidly in recent years because they provide the opportunity to study many aspects of Rydberg physics related to, for example, two-electron excited states, the properties of ultra-long-range Rydberg molecules, and Rydberg dressing and the control of few- and many-body interacting systems. Recent advances have exploited some, but by no means all, of these opportunities and this, coupled with the many questions that this earlier work has raised, suggests that interest in the alkaline-earths will only continue to grow in the future.

Acknowledgments

It is a pleasure to acknowledge the help of X Zhang, J A Aman, and F Camargo in the preparation of figures for this article. The research by the authors and their colleagues described here was supported by the NSF under grants Nos. 1301773 and 1205946, by the AFOSR under grant No. FA9550-12-1-0267, by the Robert A. Welch Foundation under grants Nos. C-0734 and C-1844, and by the FWF (Austria) under grant No. P23359-N16 and by the FWF-SFB-049 NextLite.

References

[1] Lukin M D, Fleischhauer M, Cote R, Duan L M, Jaksch D, Cirac J I and Zoller P 2001 *Phys. Rev. Lett.* **87** 037901
[2] Urban E, Johnson T A, Henage T, Isenhower L, Yavuz D D, Walker T G and Saffman M 2009 *Nat. Phys.* **5** 110
[3] Gaëtan A, Miroshnychenko Y, Wilk T, Chotia A, Viteau M, Comparat D, Pillet P, Browaeys A and Grangier P 2009 *Nat. Phys.* **5** 115
[4] Heidemann R, Raitzsch U, Bendkowsky V, Butscher B, Löw R, Santos L and Pfau T 2007 *Phys. Rev. Lett.* **99** 163601
[5] Saffman M, Walker T G and Mølmer K 2010 *Rev. Mod. Phys.* **82** 2313
[6] Weimer H, Löw R, Pfau T and Büchler H P 2008 *Phys. Rev. Lett.* **101** 250601
[7] Pohl T, Demler E and Lukin M D 2010 *Phys. Rev. Lett.* **104** 043002
[8] Schachenmayer J, Lesanovsky I, Micheli A and Daley A J 2010 *New J. Phys.* **12** 103044
[9] Pritchard J D, Maxwell D, Gauguet A, Weatherill K J, Jones M P A and Adams C S 2010 *Phys. Rev. Lett.* **105** 193603
[10] Henkel N, Nath R and Pohl T 2010 *Phys. Rev. Lett.* **104** 195302
[11] Honer J, Weimer H, Pfau T and Büchler H P 2010 *Phys. Rev. Lett.* **105** 160404
[12] Johnson J E and Rolston S L 2010 *Phys. Rev.* A **82** 033412
[13] Balewski J B, Krupp A T, Gaj A, Hofferberth S, Löw R and Pfau T 2014 *New J. Phys.* **16** 063012
[14] Jau Y Y, Hankin A M, Keating T, Deutsch I H and Biedermann G W 2016 *Nature Phys.* **12** 71
[15] Gil L I R, Mukherjee R, Bridge E M, Jones M P A and Pohl T 2014 *Phys. Rev. Lett.* **112** 103601
[16] Derevianko A and Katori H 2011 *Rev. Mod. Phys.* **83** 331
[17] Ludlow A D, Boyd M M, Ye J, Peik E and Schmidt P O 2015 *Rev. Mod. Phys.* **87** 637
[18] Pisharody S N and Jones R R 2004 *Science* **303** 813
[19] Mukherjee R, Millen J, Nath R, Jones M P A and Pohl T 2011 *J. Phys.* B **44** 184010
[20] Percival I C 1977 *Proc. R. Soc. London* A **353** 289
[21] Tanner G, Richter K and Rost J M 2000 *Rev. Mod. Phys.* **72** 497
[22] Kalinski M, Eberly J H, West J A and Stroud C R 2003 *Phys. Rev.* A **67** 032503
[23] Qiu Y, Müller J and Burgdörfer J 1996 *Phys. Rev.* A **54** 1922
[24] Gallagher T F 1994 *Rydberg Atoms* (Cambridge: Cambridge University Press)
[25] Stellmer S, Schreck F and Killian T C 2014 *Annual Review of Cold Atoms and Molecules vol 2* ed K W Madison *et al* (Singapore: World Scientific)
[26] Mickelson P G, Martinez de Escobar Y N, Yan M, DeSalvo B J and Killian T C 2010 *Phys. Rev.* A **81** 051601
[27] Stellmer S, Grimm R and Schreck F 2013 *Phys. Rev.* A **87** 013611
[28] Vaillant C L, Jones M P A and Potvliege R M 2014 *J. Phys. B: At. Mol. Opt. Phys* **47** 155001

[29] Vaillant C L, Jones M P A and Potvliege R M 2012 *J. Phys. B: At. Mol. Opt. Phys* **45** 135004
[30] Aymar M, Greene C H and Luc-Koenig E 1996 *Rev. Mod. Phys.* **68** 1015
[31] Seaton M J 1983 *Rep. Prog. Phys.* **46** 167
[32] Ye S, Zhang X, Killian T C, Dunning F B, Hiller M, Yoshida S, Nagele S and Burgdörfer J 2013 *Phys. Rev.* A **88** 043430
[33] Millen J, Lochead G, Corbett G R, Potvliege R M and Jones M P A 2011 *J. Phys. B: At. Mol. Opt. Phys* **44** 184001
[34] Millen J, Lochead G and Jones M P A 2010 *Phys. Rev. Lett.* **105** 213004
[35] Hiller M, Yoshida S, Burgdörfer J, Ye S, Zhang X and Dunning F B 2014 *Phys. Rev.* A **89** 023426
[36] Ye S, Zhang X, Dunning F B, Yoshida S, Hiller M and Burgdörfer J 2014 *Phys. Rev.* A **90** 013401
[37] Dunning F B, Mestayer J J, Reinhold C O, Yoshida S and Burgdörfer J 2009 *J. Phys. B: At. Mol. Opt. Phys* **42** 022001
[38] Dunning F B, Reinhold C O, Yoshida S and Burgdörfer J 2010 *Am. J. Phys.* **78** 796
[39] Wyker B, Ye S, Dunning F B, Yoshida S, Reinhold C O and Burgdörfer J 2012 *Phys. Rev. Lett.* **108** 043001
[40] Zhang X, Dunning F B, Yoshida S and Burgdörfer J 2015 *Phys. Rev.* A **92** 051402
[41] Greene C H, Dickinson A S and Sadeghpour H R 2000 *Phys. Rev. Lett.* **85** 2458–61
[42] Bendkowsky V, Butscher B, Nipper J, Shaffer J P, Löw R and Pfau T 2009 *Nature* **458** 1005
[43] Li W *et al* 2011 *Science* **334** 1110
[44] Tallant J, Rittenhouse S T, Booth D, Sadeghpour H R and Shaffer J P 2012 *Phys. Rev. Lett.* **109** 173202
[45] Bellos M A, Carollo R, Banerjee J, Eyler E E, Gould P L and Stwalley W C 2013 *Phys. Rev. Lett.* **111** 053001
[46] Anderson D A, Miller S A and Raithel G 2014 *Phys. Rev. Lett.* **112** 163201
[47] Krupp A T, Gaj A, Balewski J B, Ilzhöfer P, Hofferberth S, Löw R, Pfau T, Kurz M and Schmelcher P 2014 *Phys. Rev. Lett.* **112** 143008
[48] Saßmannshausen H, Merkt F and Deiglmayr J 2015 *Phys. Rev. Lett.* **114** 133201
[49] Gaj A, Krupp A T, Ilzhöfer P, Löw R, Hofferberth S and Pfau T 2015 *Phys. Rev. Lett.* **115** 023001
[50] Booth D, Rittenhouse S T, Yang J, Sadeghpour H R and Shaffer J P 2015 *Science* **348** 99
[51] Eiles M T and Greene C H 2015 *Phys. Rev. Lett.* **115** 193201
[52] Gaj A, Krupp A T, Balewski J B, Löw R, Hofferberth S and Pfau T 2014 *Nat. Commun.* **5** 5546
[53] DeSalvo B J, Aman J A, Dunning F B, Killian T C, Sadeghpour H R, Yoshida S and Burgdörfer J 2015 *Phys. Rev.* A **92** 031403
[54] Balewski J B, Krupp A T, Gaj A, Peter D, Bchler H P, Löw R, Hofferberth S and Pfau T 2013 *Nature* **502** 664 ISSN 00280836
[55] Karpiuk T, Brewczyk M, Rążewski K, Gaj A, Balewski J B, Krupp A T, Schlagmüller M, Löw R, Hofferberth S and Pfau T 2015 *New J. Phys.* **17** 053046
[56] Butscher B, Bendkowsky V, Nipper J, Balewski J B, Kukota L, Löw R, Pfau T, Li W, Pohl T and Rost J M 2011 *J. Phys. B: At. Mol. Opt. Phys* **44** 184004
[57] Camargo F, Whalen J D, Ding R, Sadeghpour H R, Yoshida S, Burgdörfer J, Dunning F B and Killian T C 2015 *Phys. Rev.* A **93** 022702 2016
[58] Helmrich S, Arias A, Pehoviak N and Whitlock S 2016 *J. Phys. B: At. Mol. Opt. Phys* **49** 03LT02
[59] Glaetzle A W, Dalmonte M, Nath R, Gross C, Bloch I and Zoller P 2015 *Phys. Rev. Lett.* **114** 173002
[60] van Bijnen R M W and Pohl T 2015 *Phys. Rev. Lett.* **114** 243002
[61] Maucher F, Henkel N, Saffman M, Królikowski W, Skupin S and Pohl T 2011 *Phys. Rev. Lett.* **106** 170401
[62] Pupillo G, Micheli A, Boninsegni M, Lesanovsky I and Zoller P 2010 *Phys. Rev. Lett.* **104** 223002
[63] Boninsegni M and Prokof'ev N V 2012 *Rev. Mod. Phys.* **84** 759
[64] Hughey T R, Kleppner B J, Ducas D and Gentile T W 1989 *Phys. Rev.* A **40** 5103
[65] Schempp H *et al* 2014 *Phys. Rev. Lett.* **112** 013002
[66] Malossi N, Valado M M, Scotto S, Morsch O, Arimondo E and Ciampini D 2014 *J. Phys.: Conf. Ser.* **497** 012031
[67] Wang T, Yelin S F, Côté R, Eyler E E, Farooqi S M, Gould P L, Koštrun M, Tong D and Vrinceanu D 2007 *Phys. Rev.* A **75** 033802
[68] Weatherill K J, Pritchard J D, Abel R P, Bason M G, Mohapatra A K and Adams C S 2008 *J. Phys. B: At. Mol. Opt. Phys* **41** 201002
[69] Goldschmidt E A, Boulier T, Brown R C, Koller S B, Young J T, Gorshkov A V, Rolston S L and Porto J V 2016 *Phys. Rev. Lett.* **116** 113001
[70] Raitzsch U, Heidemann R, Weimer H, Butscher B, Kollmann P, Löw R, Büchler H P and Pfau T 2009 *New J. Phys.* **11** 055014
[71] Zeiher J, Schauß P, Hild S, Macrı′ T, Bloch I and Gross C 2015 *Phys. Rev.* X **5** 031015
[72] Schempp H, Günter G, Hofmann C S, Giese C, Saliba S D, DePaola B D, Amthor T, Weidemüller M, Sevinçli S and Pohl T 2010 *Phys. Rev. Lett.* **104** 173602
[73] Sevinçli S *et al* 2011 *J. Phys.* B **44** 184018
[74] Zhang H, Zhang L, Wang L, Bao S, Zhao J, Jia S and Raithel G 2014 *Phys. Rev.* A **90** 043849
[75] DeSalvo B J, Aman J A, Gaul C, Pohl T, Yoshida S, Burgdörfer J, Hazzard K R A, Dunning F B and Killian T C 2015 *Phys. Rev.* A **93** 022709
[76] Gaul C, DeSalvo B J, Aman J A, Dunning F B, Killian T C and Pohl T 2015 (arXiv:1511.06424)
[77] Robinson M P, Tolra B L, Noel M W, Gallagher T F and Pillet P 2000 *Phys. Rev. Lett.* **85** 4466
[78] Robicheaux F 2005 *J. Phys.* B **38** S333
[79] Killian T C, Pattard T, Pohl T and Rost J M 2007 *Phys. Rep.* **449** 77
[80] Schwarzkopf A, Sapiro R E and Raithel G 2011 *Phys. Rev. Lett.* **107** 103001
[81] McQuillen P, Zhang X, Strickler T, Dunning F B and Killian T C 2013 *Phys. Rev.* A **87** 013407
[82] Bannasch G, Killian T C and Pohl T 2013 *Phys. Rev. Lett.* **110** 253003
[83] Killian T C, Ashoka V S, Gupta P, Laha S, Nagel S B, Simien C E, Kulin S, Rolston S L and Bergeson S D 2003 *J. Phys. A: Math. Gen.* **36** 6077
[84] Lyon M, Bergeson S D, Diaw A and Murillo M S 2015 *Phys. Rev.* E **91** 033101